Journal of the Optical Society of America A
OPTICS, IMAGE SCIENCE, AND VISION

Wideband image demodulation via bi-dimensional multirate frequency transformations

Wenjing Liu* and Balu Santhanam

Department of Electrical & Computer Engineering, University of New Mexico, MSC01 1100, 1 University of New Mexico, Albuquerque, New Mexico 87131-0001, USA
**Corresponding author: wenjing@unm.edu*

Received 15 February 2016; revised 15 June 2016; accepted 27 June 2016; posted 30 June 2016 (Doc. ID 259217); published 4 August 2016

Existing image demodulation approaches based on the two-dimensional (2D) multicomponent AM–FM model assume narrowband components that can be demodulated using energy operators, Hilbert transforms, or the monogenic image approaches. However, if the FM components are wideband, then these demodulation approaches incur significant errors. Recent work by the authors extended wideband FM demodulation in one dimension to accommodate large conversion factors using multirate frequency transformations. In this paper, we extend the multirate frequency transformations technique developed for one-dimensional signals to 2D and images in conjunction with a recently proposed 2D higher-order energy demodulation approach. This extension is applied to both synthetic and real images to demonstrate the efficacy of the approach.

OCIS codes: (100.2000) Digital image processing; (100.2960) Image analysis.

http://dx.doi.org/10.1364/JOSAA.33.001668

1. INTRODUCTION

The amplitude-modulation frequency-modulation (AM–FM) representation model has found various applications with images, recently including image analysis, texture processing [1], and fingerprint classification [2]. According to earlier work [3,4] by Havlicek *et al.*, non-stationary images can be modeled as superpositions of multiple AM–FM components,

$$I(x,y) = \sum_{i=1}^{n} a_i(x,y)\cos(\phi_i(x,y)). \tag{1}$$

The multi-component AM–FM image is first decomposed by employing a set of bandpass filters such as Garbor filterbanks or via the use of the *bi-dimensional empirical mode decompostion* (BEMD) [5]. Each resulting monocomponent AM–FM image is further demodulated into the corresponding instantaneous amplitude (IA) $a(x,y)$ and instantaneous frequency vector (IF),

$$\nabla\phi(x,y) = \left[\frac{\partial\phi(x,y)}{\partial x}, \frac{\partial\phi(x,y)}{\partial y}\right]^T. \tag{2}$$

In particular, the IA depicts the contrast present in the image, while the IF reveals the locally emergent frequency variation. Conventional image demodulation approaches involve two-dimensional (2D) extension of the analytic signal (AS) [6] and multidimensional energy separation algorithm (ESA) [7] with additional processing techniques such as *dominant component analysis* (DCA) [8,9]. Recently, a monogenic image approach using the Riesz–Laplace wavelet [10–12] was also proposed.

However, in most of these approaches, narrowband assumptions were imposed on each AM–FM component of the image. For example, most literature inexplicitly assumes the AM–FM image to be globally wideband, yet each of its components to be locally narrowband. In general, both the IA $a(x,y)$ and the IF $\nabla\phi(x,y)$ of a single component are assumed to be slowly varying; otherwise, the approximations inherent in most demodulation approaches are no longer valid and incur significant errors, especially under the wideband scenario.

In this paper, we propose a novel approach called the *bi-dimensional multirate frequency transformations* (BMFT) that can be combined with a variety of demodulation techniques to enhance their demodulation performance, traditionally limited by the narrowband constraint on the frequency modulation part of the monocomponent AM–FM image.

2. WIDEBAND FREQUENCY MODULATED IMAGE

The wideband FM signal in one dimension (1D) is usually characterized by a set of parameters, such as the modulation index, carrier-to-information-bandwidth ratio (CR/IB), and carrier-to-deviation ratio (CR/FD), as defined in Ref. [13]. For example, a sinusoidal FM signal is of the form

$$x(t) = a(t)\cos\left(\int_{-\infty}^{t}[\omega_c + \omega_m\cos(\omega_f\tau+\theta)]\mathrm{d}\tau\right). \tag{3}$$

The set of parameters are then given by

$$\beta = \omega_m/\omega_f, \qquad \frac{\mathrm{CR}}{\mathrm{IB}} = \frac{\omega_c}{\omega_f}, \qquad \frac{\mathrm{CR}}{\mathrm{FD}} = \frac{\omega_c}{\omega_m}, \tag{4}$$

where β denotes the modulation index. When $\beta \gg 1$ is satisfied, such an FM signal is classified as wideband according to the literature of FM communication systems. Additionally, the performance of any demodulation algorithm is also affected by the CR/IB and the CR/FD parameters. Specifically, according to Potamianos and Maragos [14], the demodulation performance of the Hilbert transform is invariant to CR/IB, while the ESA performs better at a higher CR/IB. As for the CR/FD, most demodulation algorithms are only valid when the CR/FD is high, in which case, the deviation is small compared to the carrier frequency. Though these parameters are well defined in 1D, we cannot directly extend their definitions to 2D, since FM images are not globally separable. For instance, we are not able to define the corresponding modulation index along any specific direction for 2D images in a global sense.

However, as proposed by Pattichis and Bovik [15], the complex FM image can be locally approximated by the product of two 1D FM signals. The corresponding 1D signals are defined along the directions of the eigenvectors of the *instantaneous frequency gradient tensor* (IFGT), which is simply the Hessian of the phase. Let $\mathbf{z} = [z_1, z_2]$ denote the representation under the eigenvector coordinate system, $\widetilde{\phi}(\mathbf{z})$ denote the phase of the FM image, and $\widetilde{\mathbf{F}}$ denote the IFGT. According to Ref. [15], around a given point $\mathbf{z}_0 = [a_1, a_2]$ of the image, the local phase is approximated using a Taylor series expansion by

$$\widetilde{\phi}(\mathbf{z}) \approx \widetilde{\phi}(a_1, a_2) + \widetilde{\phi_1}(z_1) + \widetilde{\phi_2}(z_2), \tag{5}$$

where

$$\widetilde{\phi}_i(z_i) = \frac{\partial \widetilde{\phi}}{\partial z_i}(a_1, a_2)(z_i - a_i) + \frac{\lambda_i(a_1, a_2)}{2}(z_i - a_i)^2, \qquad i = 1, 2. \tag{6}$$

Note that λ_1 and λ_2 are the eigenvalues of $\widetilde{\mathbf{F}}$. The complex FM image is then locally approximated by the product of two 1D FM functions defined with respect to the eigenvector coordinate directions:

$$\exp[j\widetilde{\phi}(z_1, z_2)] \approx \exp[j\phi_1(z_1)]\exp[j\phi_2(z_2)]. \tag{7}$$

As a result, FM images can be viewed as locally separable, and we can define the wideband FM images locally by deriving the corresponding parameters along the eigenvector coordinate directions. For example, if the modulation index along the directions of the IFGT eigenvectors are sufficiently large around the reference point, the image can be expected to exhibit a similar wideband pattern locally analogous to the 1D case. Assume the modulation indexes along both directions of the eigenvectors are denoted by β_{z_1} and β_{z_2}, respectively. To locally indicate whether an FM image is wideband or not in the sense similar to the literature in FM communication systems, we can define a local modulation index β_l via

$$\beta_l = (\beta_{z_1}^2 + \beta_{z_2}^2)^{1/2}. \tag{8}$$

If β_l is sufficiently large, then the corresponding FM image exhibits a wideband pattern locally. This definition of the local modulation index β_l is especially effective for the sinusoidal FM images with IF components specified along the horizontal and vertical directions. In this case, the modulation index for each eigenvector direction can be well defined according to the original formulation in the 1D context.

3. PARTIAL HILBERT TRANSFORM DEMODULATION

The partial or directional Hilbert transform based on the analytic image as summarized in Ref. [16] by Havlicek *et al.* is widely used for monocomponent AM–FM image demodulation.

For a one-dimensional real-valued signal $s(t)$:$\mathbb{R} \to \mathbb{R}$, we associate with it an complex-valued signal $z(x) = s(x) + jq(x)$, where the imaginary part $q(t)$ is defined via

$$q(t) = \mathcal{H}[s(t)] = s(t) * \frac{1}{\pi t} = \int_{\mathbb{R}} \frac{s(t-\xi)}{\pi\xi}\mathrm{d}\xi. \tag{9}$$

Note that $q(t)$ is the Hilbert transform (HT) of $s(t)$, and the complex-valued signal $z(t)$ is called the analytic signal. Assume that $s(t)$ is a real-valued AM–FM signal given by

$$s(t) = a(t)\cos(\omega_c t + \phi(t)), \tag{10}$$

where $a(t)$ is the IA, ω_c is the carrier frequency, and $\phi(t)$ is the phase for the IF $\phi'(t)$. According to the basic property of the Hilbert transform and *Bedrosian's theorem*, $q(t)$ is a natural approximation to the product of the IA $a(t)$ and the quadrature of $\cos(\omega_c t + \phi(t))$ given by

$$q(t) = \mathcal{H}[s(t)] \approx a(t)\sin(\omega_c t + \phi(t)). \tag{11}$$

However, this approximation is valid only if the following conditions hold: (1) $a(t)$ is a narrowband low-pass signal that varies slowly with time, and (2) the carrier frequency ω_c is sufficiently large such that

$$\omega_c \gg \phi'(t). \tag{12}$$

If these narrowband conditions are met, then the corresponding analytic signal is an accurate approximation to the desired complex signal given by

$$z(t) = s(t) + jq(t) \approx a(t)\exp[j(\omega_c t + \phi(t))]. \tag{13}$$

Hence, the IA $a(t)$ and the IF $\phi'(t)$ are approximated, respectively, by

$$\widehat{a}(t) \approx \|z(t)\|, \tag{14}$$

$$\widehat{\phi}'(t) \approx \frac{\partial}{\partial t}\left(\arctan\frac{\Im(z(t))}{\Re(z(t))}\right) - \omega_c. \tag{15}$$

Such a process can be extended to 2D via the partial Hilbert transform. Let $f(\mathbf{x})$:$\mathbb{R}^n \to \mathbb{R}$ and $\mathbf{e}_i$ denote the unit vector in the x_i direction. The partial Hilbert transform along the direction of $\mathbf{e}_i$ is then defined by

$$\mathcal{H}_{x_i}[f(\mathbf{x})] = \int_{\mathbb{R}} \frac{f(\mathbf{x} - \xi\mathbf{e}_i)}{\pi\xi}\mathrm{d}\xi. \tag{16}$$

Note that the partial Hilbert transform defined here is specified along the horizontal and vertical directions. Thus, it is particularly suitable for demodulating images with frequency modulation patterns emerging along the same directions. Assume that $I(x, y)$ is a monocomponent AM–FM image with

frequency modulation patterns emerging along both the horizontal and vertical directions given by

$$I(x,y) = A(x,y)\cos(\Omega_x x + \Omega_y y + \varphi(x,y)), \tag{17}$$

where Ω_x and Ω_y denote the carrier (mean) frequencies along the x and y directions, respectively. (According to Refs. [4,17], we interpret the IF as a variation about the mean frequency. Ω_x and Ω_y can be explained as the carrier frequencies of the visual information. Based on this consideration, the uniqueness problem of the IF and IA can be resolved under certain conditions.) Under this assumption, according to Eq. (11), we are able to approximate the partial Hilbert transform along the x-axis by fixing variable y via

$$\mathcal{H}_x[I(x,y)] \approx A(x,y)\sin(\Omega_x x + (\Omega_y y + \varphi(x,y))). \tag{18}$$

This approximation holds only under certain conditions similar to the 1D case. First of all, the AM part $A(x,y)$ should be slow varying and narrowband. Analogous to Eq. (12), Ω_x is required to be sufficiently large such that

$$\Omega_x \gg \frac{\partial\varphi(x,y)}{\partial x}. \tag{19}$$

A similar condition applies to the y-axis as well. As a result, we can easily obtain the approximations for the IA and the IF components with respect to both directions, according to the 2D extensions of Eqs. (14) and (15).

In Section 7, synthetic examples are provided to illustrate the efficacy of the proposed approach. Since the synthetic images we present are predefined, with their frequency modulation patterns along the horizontal and vertical directions, the partial Hilbert transform is preferred over the monogenic image approach to serve as the comparison technique to the proposed approach due to the following reasons: (1) the demodulation performance of the partial Hilbert transform is as competitive as the Riez transform when the image displays frequency modulation patterns along the same specified directions, and (2) the partial Hilbert transform can be implemented easily via the 1D Hilbert transform.

4. HIGHER-ORDER ENERGY OPERATOR

A variety of methods based on the multidimensional energy operator [7] proposed by Maragos and Bovik are also widely used for AM–FM image demodulation. An image demodulation algorithm based on higher-order Teager–Kaiser operators is proposed in the recent work [18–20] by Salzenstein and coworkers. They have been reported to provide better performance for narrowband AM–FM images than the classical 2D ESA [7].

The k-order differential energy operator (DEO) [21,22] in 1D for any given signal $s(t)$ is defined by

$$\Psi_k[s(t)] = \frac{\partial s(t)}{\partial t}\frac{\partial^{k-1}s(t)}{\partial t^{k-1}} - s(t)\frac{\partial^k s(t)}{\partial t^k}, \tag{20}$$

where Ψ_2 refers to the commonly used Teager–Kaiser energy operator. For a given image $I(k,l)$, the discrete-time higher-order demodulation algorithm (DHODA) [18–20] can be summarized via

$$I_1(k,l) = \frac{1}{2}[I(k+1,l) - I(k-1,l)], \tag{21}$$

$$I_2(k,l) = \frac{1}{2}[I(k,l+1) - I(k,l-1)], \tag{22}$$

$$I_{12}(k,l) = \frac{1}{2}[I_2(k+1,l) - I_2(k-1,l)], \tag{23}$$

$$\begin{aligned}\Psi_2[I(k,l)] = \{&2[I(k,l)]^2 - I(k-1,l)I(k+1,l)\\ &- I(k,l-1)I(k,l+1)\} + 2[I_1(k,l)I_2(k,l)\\ &- I(k,l)I_{12}(k,l)],\end{aligned} \tag{24}$$

$$I_{12}^1(k,l) = \frac{1}{2}[I_{12}(k+1,l) - I_{12}(k-1,l)], \tag{25}$$

$$I_{12}^2(k,l) = \frac{1}{2}[I_{12}(k,l+1) - I_{12}(k,l-1)], \tag{26}$$

$$|\widehat{a}(k,l)| = \left(\frac{\Psi_2[I_1(k,l)]\Psi_2[I_2(k,l)]}{\Psi_2[I_{12}^1(k,l) + I_{12}^2(k,l)]}\right)^{1/2}, \tag{27}$$

$$|\widehat{\Omega}_1(k,l)| = \arcsin\left(\left(\frac{\Psi_2[I_{12}(k,l)]}{\Psi_2[I_2(k,l)]}\right)^{1/2}\right), \tag{28}$$

$$|\widehat{\Omega}_2(k,l)| = \arcsin\left(\left(\frac{\Psi_2[I_{12}(k,l)]}{\Psi_2[I_1(k,l)]}\right)^{1/2}\right), \tag{29}$$

where $\widehat{a}(k,l)$ is the IA estimation, while $\widehat{\Omega}_1(k,l)$ and $\widehat{\Omega}_2(k,l)$ are the IF estimations along the spatial axis of the image. Note that the IF estimations are obtained through the inverse sine function, indicating that the demodulation approaches based on the ESA can only estimate IF components that range between 0 and $\frac{\pi}{2}$, or in other words, up to one-fourth of the sampling frequency. Moreover, the demodulation approaches based on the ESA also suffer from the narrowband constraint like the Hilbert transform. Both the IA and the IF waveforms may not vary too fast or too greatly in value.

5. BI-DIMENSIONAL MULTIRATE FREQUENCY TRANSFORMATIONS

The *multirate frequency transformations* (MFT) approach that performs wideband-to-narrowband conversion of an FM signal was proposed in a prior work [23]. The MFT primarily increases the CR/IB and CR/FD ratios of the original signal to improve upon the demodulation performance of the conventional demodulation approaches. The BMFT is derived by generalizing the underlying idea to 2D. For simplicity, assume that the input is a monocomponent wideband FM image of the form

$$J(x,y) = A\cos(\phi(x,y)). \tag{30}$$

It is first compressed in the frequency domain by the appropriate factors $\mathbf{R} = \mathrm{diag}[R_x, R_y]$, which correspond to the spatial expansion given by

$$J_1(x,y) = A\cos\left(\phi\left(\frac{x}{R_x},\frac{y}{R_y}\right)\right). \tag{31}$$

Then, we heterodyne the resultant image by a frequency translation vector $\Omega = [\Omega_x, \Omega_y]$ via

$$\begin{aligned} J_2(x,y) &= J_1(x,y)\cos(\Omega_x x)\cos(\Omega_y y) \\ &= \frac{A}{2}\cos\left(\Omega_x x + \phi\left(\frac{x}{R_x},\frac{y}{R_y}\right)\right)\cos(\Omega_y y) \\ &\quad + \frac{A}{2}\cos\left(\Omega_x x - \phi\left(\frac{x}{R_x},\frac{y}{R_y}\right)\right)\cos(\Omega_y y) \\ &= \frac{A}{4}\cos\left(\Omega_x x + \Omega_y y + \phi\left(\frac{x}{R_x},\frac{y}{R_y}\right)\right) \\ &\quad + \frac{A}{4}\cos\left(\Omega_x x - \Omega_y y + \phi\left(\frac{x}{R_x},\frac{y}{R_y}\right)\right) \\ &\quad + \frac{A}{4}\cos\left(\Omega_x x + \Omega_y y - \phi\left(\frac{x}{R_x},\frac{y}{R_y}\right)\right) \\ &\quad + \frac{A}{4}\cos\left(\Omega_x x - \Omega_y y - \phi\left(\frac{x}{R_x},\frac{y}{R_y}\right)\right). \end{aligned} \tag{32}$$

After the heterodyning, a 2D bandpass filter is applied to extract the desired high-frequency term through

$$\begin{aligned} \widetilde{J}(x,y) &= J_2(x,y) * h_{\mathrm{BP}}(x,y) \\ &\approx \frac{A}{4}\cos\left(\Omega_x x + \Omega_y y + \phi\left(\frac{x}{R_x},\frac{y}{R_y}\right)\right) \\ &= \frac{A}{4}\cos(\widetilde{\phi}(x,y)). \end{aligned} \tag{33}$$

Assume that the support of the original image spectrum $J(\omega_1,\omega_2)$ is within the range $\omega_i \in [-\Omega_i, \Omega_i]$, $i = 1, 2$. The 2D bandpass filter should be carefully designed, with its passband range given by

$$|\omega_1| \in \left[\Omega_x, \Omega_x + \frac{\Omega_1}{R_x}\right], \qquad |\omega_2| \in \left[\Omega_y, \Omega_y + \frac{\Omega_2}{R_y}\right]. \tag{34}$$

On one hand, the carrier (or mean) frequencies of the modulation in both dimensions are increased via the frequency translation vector $\Omega = [\Omega_x, \Omega_y]$. On the other hand, the bandwidth of the modulating image is reduced by the appropriate conversion factors $\mathbf{R} = \mathrm{diag}[R_x, R_y]$. These two benefits derived via the BMFT are crucial to improving the IF demodulation due to the following reasons: (1) a majority of demodulation approaches require the input to have high CR/IB in both dimensions, and (2) the CR/FD of the input must be sufficiently large in both dimensions such that the deviations of the IF components can be tolerated in accordance with the narrowband assumption of the input.

Then, we can recover the IF of the input image from the IF estimation of the transformed image $\widetilde{J}(x,y)$ via the inverse BMFT. Assume that the IF components of $J(x,y)$ and $\widetilde{J}(x,y)$ are given by

$$\Omega_1(x,y) = \frac{\partial\phi(x,y)}{\partial x}, \qquad \Omega_2(x,y) = \frac{\partial\phi(x,y)}{\partial y}, \tag{35}$$

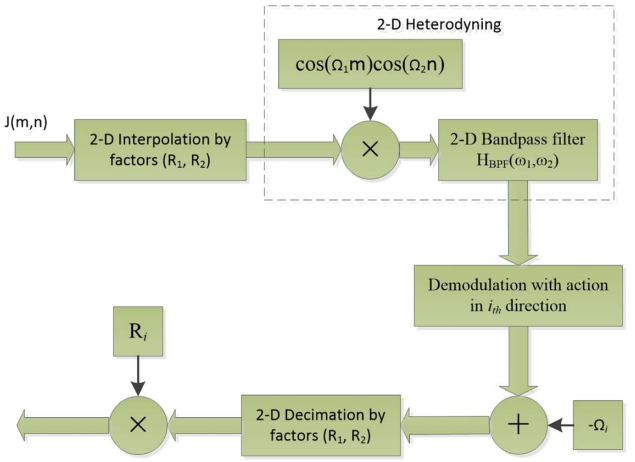

Fig. 1. Block diagram of the BMFT.

$$\widetilde{\Omega}_1(x,y) = \frac{\partial\widetilde{\phi}(x,y)}{\partial x}, \qquad \widetilde{\Omega}_2(x,y) = \frac{\partial\widetilde{\phi}(x,y)}{\partial y}. \tag{36}$$

The IF estimation for the input image is recovered through the inverse BMFT relation (see Fig. 1) via

$$\Omega_1(x,y) = R_x(\widetilde{\Omega}_1(R_x x, R_y y) - \Omega_x), \tag{37}$$

$$\Omega_2(x,y) = R_y(\widetilde{\Omega}_2(R_x x, R_y y) - \Omega_y), \tag{38}$$

where $\widetilde{\Omega}_1(R_x x, R_y y)$ and $\widetilde{\Omega}_2(R_x x, R_y y)$ represent the spatial compression (or frequency expansion) of the IF estimation for the transformed image $\widetilde{J}(x,y)$.

In order to implement the BMFT in discrete time, we replace compression and expansion in frequency domain by their discrete equivalences. Note that compression in the frequency domain corresponds to interpolation, while the expansion corresponds to decimation. As a result, the block diagram of the BMFT demodulation approach is depicted in Fig. 1. The BMFT is implemented through discrete-time operations of interpolation, heterodyning, and bandpass filtering. The transformed FM image is then demodulated via a monocomponent demodulation approach, and the original IF components are recovered from the IF estimation of the transformed image via the inverse BMFT. However, discrete-time operations in 2D may not be extended in a straightforward way from their 1D counterpart. It depends primarily on whether the input image is separable or not. If the image is separable, each operation of the BMFT can be implemented by simply cascading its 1D equivalence with action along each dimension. If this is not the case, we need to pay attention to a few issues associated with the non-separable nature of the image, which are often intractable. Therefore, deriving 2D operations directly from their 1D realizations is favored in terms of its simplicity for practical implementation.

In particular, the frequency upshift in heterodyning is not uniquely defined in 2D. This can be realized either through the product of two separable cosine terms $\cos(\Omega_1 m)\cos(\Omega_2 n)$ in each dimension as in Fig. 1 or via just one cosine term

$\cos(\Omega_1 m + \Omega_2 n)$ in the diagonal direction. These two different realizations will lead to different designs of the 2D bandpass filters. For the first case, we only need to bandpass filter the outermost quarter of the frequency spectrum in each quadrant to extract the desired high-frequency term expressed in Eq. (33). This is simply achieved using a separable 2D bandpass filter by cascading two 1D bandpass filters with action in each dimension. For the latter case, where the frequency upshift is diagonal, it is much more complicated to achieve the same objective with a realizable design of the 2D bandpass filter. The issue is that the 2D frequency upshift in the diagonal direction results in only two copies of the original spectrum in the first and third quadrants. However, the design of a 2D bandpass filter whose passband is only present in two quadrants and also capable of extracting the desired term in Eq. (33) is computationally complex.

In addition, the BMFT framework can be directly applied on a monocomponent AM–FM image, provided that the IA of the given image is slowly varying, which is inherently assumed by most image demodulation algorithms. Under this constraint, the IA can be approximated via the inverse BMFT relation by

$$A(x, y) = \widetilde{A}(R_x x, R_y y), \tag{39}$$

where $\widetilde{A}(x, y)$ denotes the demodulated IA of the transformed image $\widetilde{f}(x, y)$. Numerical results are given later in the paper to support this claim.

6. DISCUSSION OF THE BMFT COMPATIBILITY WITH THE HT AND ESA APPROACHES

In general, the BMFT framework can be combined with most demodulation approaches to enhance their performance in the wideband scenario. But the gain achieved by using the BMFT framework varies with the demodulation algorithm employed. For a given demodulation scheme, the gain in error reduction via the BMFT approach depends mainly on its inherent sensitivity to CR/IB, CR/FD, and the modulation index of the image. Here we refer to the comparison results of the HT approaches and ESA approaches in 1D [14] for intuitive understanding of this issue in 2D.

The HT demodulation approaches are usually not very sensitive to the CR/IB of the signal. In general, the demodulation performance of the Hilbert transform is invariant to the CR/IB of the signal. As shown in the work [14] by Potamianos and Maragos, the error versus the CR/IB response of the Hilbert transform is almost flat, suggesting that by increasing the CR/IB via the BMFT, the gain we achieve through error reduction is very limited. On the other hand, the ESA is shown to be very sensitive to the CR/IB of the signal, where the error decreases sharply as the CR/IB of the signal increases. Hence, the gain attained by increasing the CR/IB via the BMFT with demodulation schemes based on the ESA is expected to be more significant than demodulation schemes using the HT approaches.

As for the CR/FD, both the HT and ESA demodulation methods suffer from large deviation compared with the carrier frequency. Hence, the BMFT becomes beneficial to both of them via an increase in the CR/FD of the input.

Since the modulation index is jointly determined by both the CR/IB and CR/FD, its influence on the demodulation performance is not straightforward. However, the modulation index of the FM signal cannot be too large such that the spectrum of the side lobes around the origin are significant and begin to incur significant demodulation error. The theoretical analysis for this phenomenon is provided in Appendix A, where we analyze the demodulation error associated with the Hilbert transform for illustration. The error incurred due to a large modulation index is unavoidable for any demodulation algorithm. It imposes a lower bound on the demodulation error. Even the BMFT framework cannot reduce the error significantly in this extreme wideband scenario.

In conclusion, the proposed BMFT approach is more suitable for the ESA demodulation schemes. Moreover, the BMFT framework helps to overcome the estimation range constraint inherent in the ESA demodulation schemes. By compressing and shifting the original input in the frequency domain, we can always choose appropriate conversion factors and translation frequencies to convert its frequency components into the range between 0 and $\frac{\pi}{2}$. This is another advantage for combining the BMFT framework with the ESA demodulation schemes. Therefore, in the numerical experiments, we mainly focus on the BMFT and the DHODA combination to explore the benefit attained via the proposed framework and use the partial Hilbert transform as a comparison tool.

In addition, the BMFT framework can be extended in an immediately obvious separable way into multi-dimensional space and combined with the multi-dimensional higher-order differential operators recently proposed by Salzenstein and coworkers [24,25] for further study.

7. EXPERIMENTS AND SIMULATION

In this section, we present the numerical results for the proposed BMFT-energy approach. We begin with an example of a synthetic sinusoidal AM–FM image, as illustrated in Fig. 2. The expression of this synthetic image and its corresponding IF components are given by

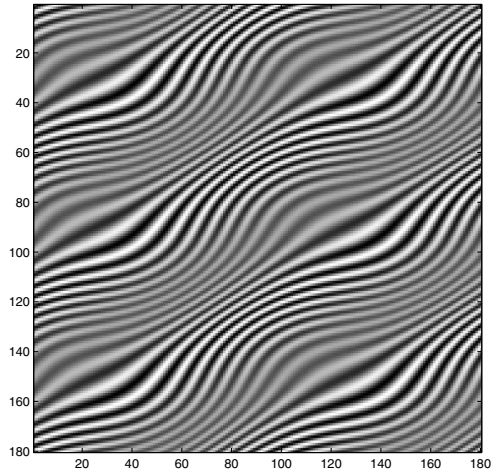

Fig. 2. Synthetic sinusoidal AM–FM image with wideband FM components of the form $f(m, n) = [1 + 0.5\cos(\frac{\pi}{50}m + \frac{\pi}{30}n)]\cos(\frac{\pi}{5}m + \frac{\pi}{3}n + 6\sin(\frac{\pi}{50}m + \frac{\pi}{2}) + 5\sin(\frac{\pi}{30}n))$.

$$f(m,n)=\left[1+0.5\cos\left(\frac{\pi}{50}m+\frac{\pi}{30}n\right)\right]\times\cos\left(\frac{\pi}{5}m+\frac{\pi}{3}n+6\sin\left(\frac{\pi}{50}m+\frac{\pi}{2}\right)+5\sin\left(\frac{\pi}{30}n\right)\right),\tag{40}$$

$$\Omega_1(m,n)=\frac{\partial\phi(m,n)}{\partial m}=\frac{\pi}{5}+\frac{3\pi}{25}\cos\left(\frac{\pi}{50}m+\frac{\pi}{2}\right),\tag{41}$$

$$\Omega_2(m,n)=\frac{\partial\phi(m,n)}{\partial n}=\frac{\pi}{3}+\frac{\pi}{6}\cos\left(\frac{\pi}{30}n\right).\tag{42}$$

Note that the frequency modulation index is 6 along the horizontal direction and 5 along the vertical direction, both of

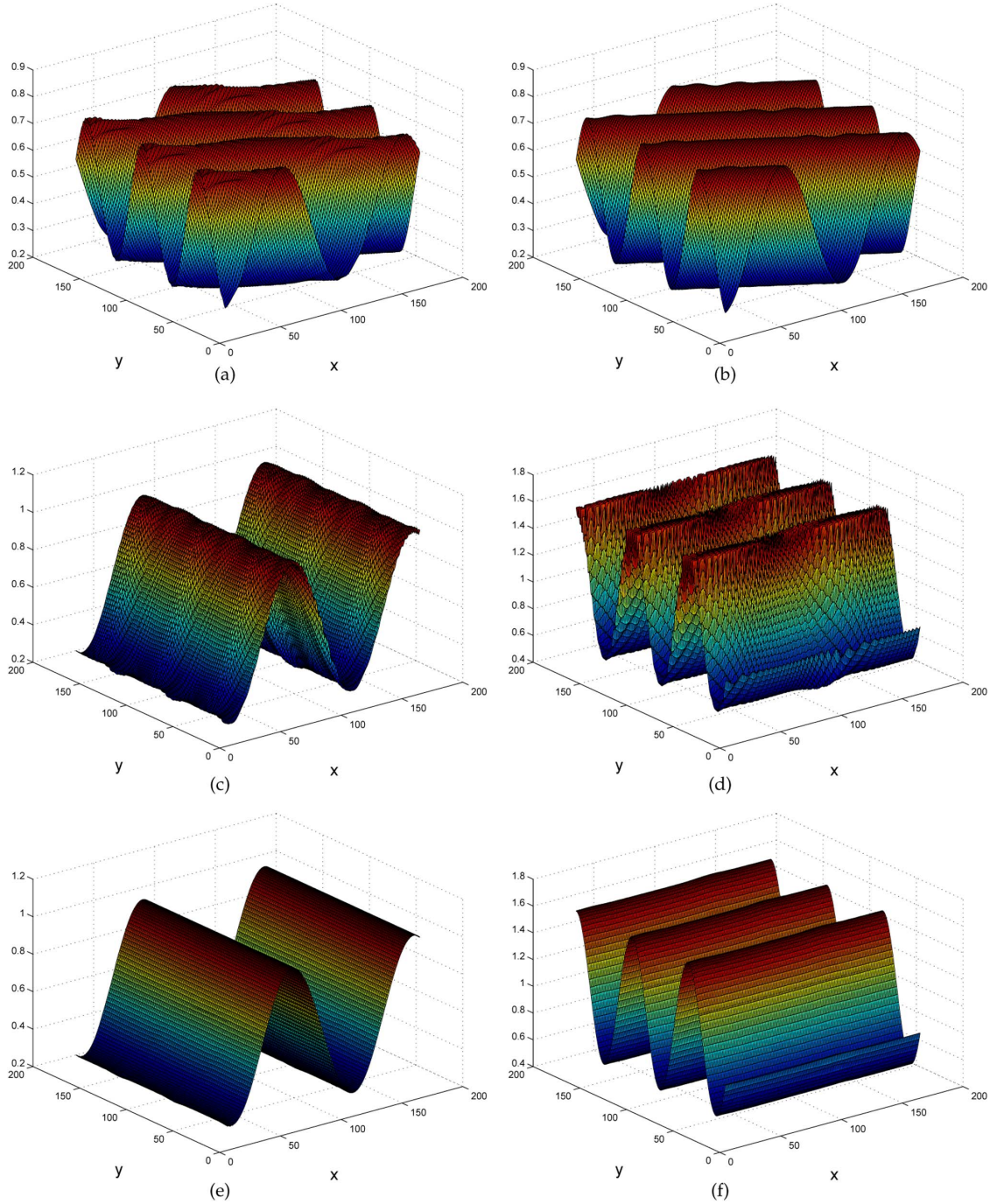

Fig. 3. Perspective plot of the demodulation results for the wideband sinusoidal example via the DHODA and via the BMFT-DHODA with conversion factors $\mathbf{R}=\mathrm{diag}[8,8]$. (a) Estimation of the IA via the DHODA, (b) estimation of the IA via the BMFT-DHODA, (c) estimation of the IF component along the horizontal direction via the DHODA, (d) estimation of the IF component along the vertical direction via the DHODA, (e) estimation of the IF component along the horizontal direction via the BMFT-DHODA, and (f) estimation of the IF component along the vertical direction via the BMFT-DHODA.

Table 1. Comparison of the Demodulation Errors

	var $(\frac{a-\hat{a}}{a})$	MSE $(a,\hat{a})$	var $(\frac{\Omega_1-\hat{\Omega}_1}{\Omega_1})$	var $(\frac{\Omega_2-\hat{\Omega}_2}{\Omega_2})$	MSE $(\Omega_1,\hat{\Omega}_1)$	MSE $(\Omega_2,\hat{\Omega}_2)$	RMSE (%)
DHODA	4.7876	0.8910	2.6688	8.0073	0.6948	12.9626	1.83
BMFT-DHODA-8	0.2934	0.0649	0.3554	0.1281	0.0427	0.1310	0.25
BMFT-DHODA-16	0.1677	0.0412	0.5608	0.0813	0.0419	0.0701	0.18
HTDA	0.5125	0.0942	0.3715	0.0683	0.1276	0.0430	0.23
BMFT-HTDA-8	0.2930	0.0646	0.1228	0.0796	0.0235	0.0716	0.20

which are sufficiently large. We can also easily check that the CR/IB and the CR/FD are small along both directions for this wideband sinusoidal example.

The demodulation results via the DHODA combined with the proposed BMFT framework using conversion factors of $\mathbf{R} = \text{diag}[8, 8]$ are given by Fig. 3. It is compared with the demodulation via the DHODA alone. Note that the demodulated IF with respect to either the horizontal or the vertical direction exhibits a sinusoidal pattern along that direction, which can be inferred from Eq. (40). We can easily observe that both the IA and the IF obtained via the BMFT-DHODA are smoother than that via the DHODA alone. The mean square error for the IA is reduced from 0.8910 to 0.0649, and the *root mean square error* (RMSE) for the IF is reduced significantly from 1.83% to 0.25% through the BMFT framework. Here we define the RMSE as the l_2 norm of the difference between the true IF $\nabla\phi(x, y)$ and the estimated IF $\nabla\widehat{\phi}(x, y)$ against the l_2 norm of the true IF itself via

$$\text{RMSE} = \frac{\|\nabla\phi(x, y) - \nabla\widehat{\phi}(x, y)\|_{l_2}}{\|\nabla\phi(x, y)\|_{l_2}} \times 100\%. \quad (43)$$

In fact, the demodulation error can be further reduced if larger multirate conversion factors are applied. As shown in Table 1, the demodulation errors of the proposed BMFT framework using DHODA with conversion factors of $\mathbf{R} = \text{diag}[8, 8]$ (BMFT-DHODA-8) and with conversion factors of $\mathbf{R} = \text{diag}[16, 16]$ (BMFT-DHODA-16) are compared with the DHODA alone. The RMSE can be further reduced to 0.18% via the BMFT with conversion factors $\mathbf{R} = \text{diag}[16.16]$, achieving an error reduction of 10 times compared with the DHODA alone. The use of larger factors results in a much narrower passband for digital filters that are difficult to realize in practice due to a sharper transition band. To implement such FIR filters, a very large filter order is required, which may not be acceptable in terms of the desired system complexity. Therefore, the choice of multirate conversion factors should be determined by weighing between the tolerance for demodulation error and that of the system complexity. Recently, the BMFT structure using large conversion factors has been implemented via an equivalent structure that alleviates the complexity of practical realization, as proposed in Ref. [26]. Aided by this equivalent structure, we may further reduce the demodulation error by exploring even larger factors.

The demodulation results via the partial Hilbert transform alone (HTDA) and the BMFT and the partial Hilbert transform combination with conversion factors $\mathbf{R} = \text{diag}[8, 8]$ (BMFT-HTDA-8) are also illustrated in Table 1. We can see that the error reduction via the BMFT framework for the HT demodulation is not as obvious as for the ESA demodulation, which justifies our discussion in the previous section.

In the second experiment, we test the BMFT and the DHODA combination on a wideband sinusoidal FM image whose IF components are out of the range $[0, \frac{\pi}{2}]$, which is the estimation range constraint for demodulation approaches based on the ESA. As shown in Fig. 4, the synthetic image for this example and its corresponding IF components are given by

$$f(m, n) = 0.5 \cos\left(\frac{2\pi}{3}m + \frac{2\pi}{3}n + 6 \sin\left(\frac{\pi}{50}m + \frac{\pi}{2}\right) + 5 \sin\left(\frac{\pi}{30}n\right)\right), \quad (44)$$

$$\Omega_1(m, n) = \frac{\partial\phi(m, n)}{\partial m} = \frac{2\pi}{3} + \frac{3\pi}{25} \cos\left(\frac{\pi}{50}m + \frac{\pi}{2}\right), \quad (45)$$

$$\Omega_2(m, n) = \frac{\partial\phi(m, n)}{\partial n} = \frac{2\pi}{3} + \frac{\pi}{6} \cos\left(\frac{\pi}{30}n\right). \quad (46)$$

Note that the carrier frequency along each direction is $\frac{2\pi}{3}$. Hence, the IF components of the image are out of the range $[0, \frac{\pi}{2}]$. The demodulation results for the DHODA and the

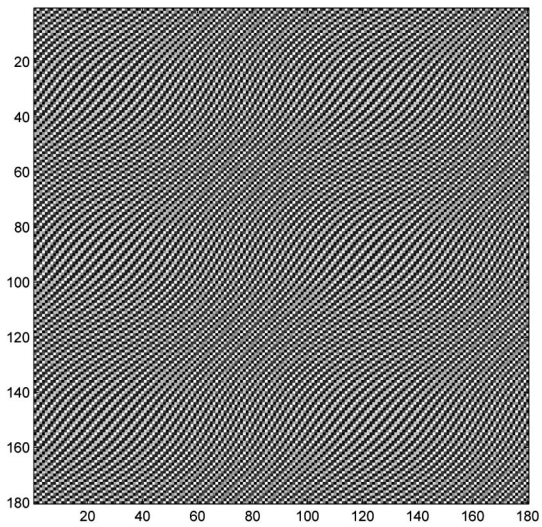

Fig. 4. Wideband sinusoidal FM image with IF components outside the range of ESA constraint $[0\frac{\pi}{2}]$ in the form $f(m, n) = 0.5 \cos(\frac{2\pi}{3}m + \frac{2\pi}{3}n + 6 \sin(\frac{\pi}{50}m + \frac{\pi}{2}) + 5 \sin(\frac{\pi}{30}n))$.

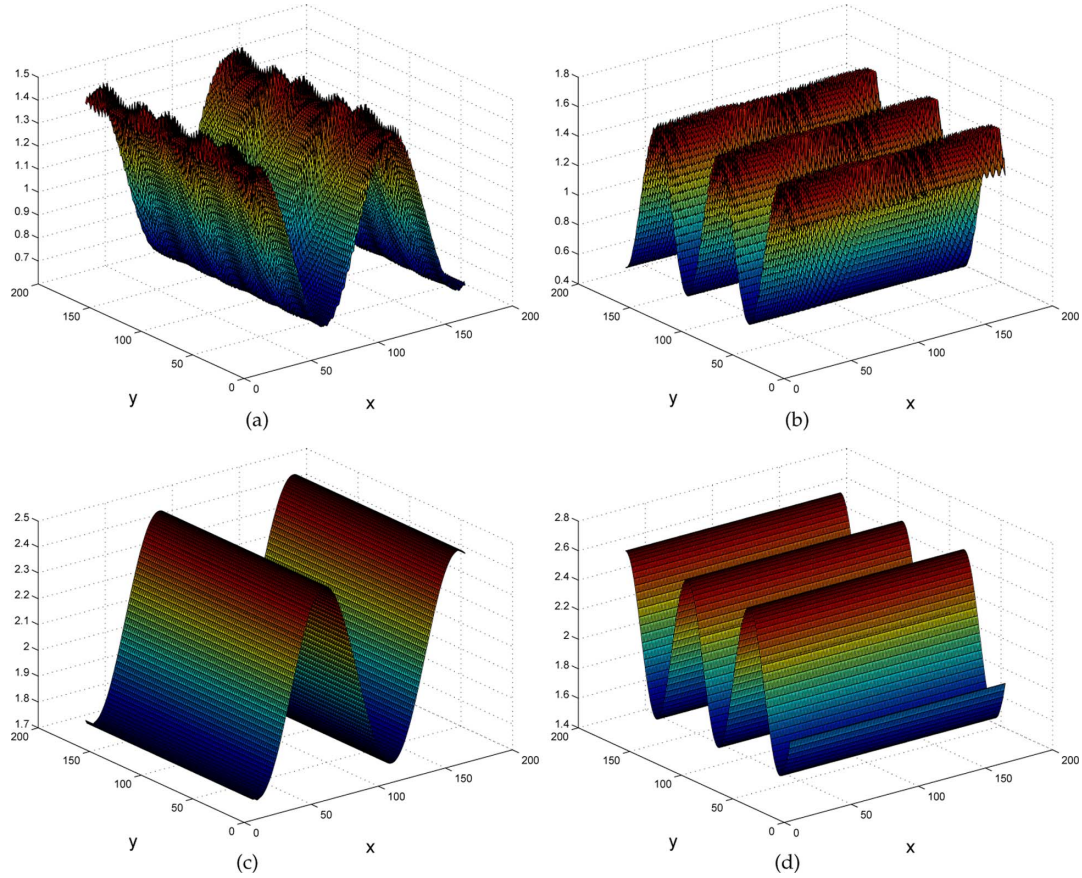

Fig. 5. Perspective plot of the IF estimation for the wideband sinusoidal example where IF components are out of the range $[0, \frac{\pi}{2}]$ via the DHODA and via the BMFT-DHODA with conversion factors $\mathbf{R} = \text{diag}[8, 8]$. (a) Estimation of the IF component along the horizontal direction via the DHODA, (b) estimation of the IF component along the vertical direction via the DHODA, (c) estimation of the IF component along the horizontal direction via the BMFT-DHODA, and (d) estimation of the IF component along the vertical direction via the BMFT-DHODA. Note that the IF estimation via the DHODA is seriously distorted in both its amplitude and phase.

BMFT-DHODA are illustrated in Fig. 5. As we can observe, the demodulated IF components via the DHODA are seriously distorted in both amplitudes and phases, whereas the demodulated IF components via the BMFT-DHODA are smooth and valid. The RMSE for the DHODA is as large as 56.74%, while the RMSE for the BMFT-DHODA is merely 0.9113%. Hence, our claim that the BMFT helps overcome the range constraint of demodulation algorithms based on ESA is justified.

In the third experiment, we justify the efficacy of the proposed BMFT approach on real images. The real image of an oak ring (photo by H. D. Grissino-Mayer from http://web.utk.edu/~grissino/index.htm) is shown in Fig. 6(a). The demodulation results associated with this real oak ring image are compared in Fig. 6. The estimated IF components via the DHODA, as shown in Figs. 6(b) and 6(c), have singular points with significantly large values. The estimated IF components via the BMFT-DHODA, as shown in Figs 6(d) and 6(e), are much smoother and do not have any singular point with a significantly large value. As a result, the estimated IF needle plot of the DHODA [Fig. 6(f)] is seriously distorted by those singular points, whereas the estimated IF needle plot of the BMFT-DHODA [Fig. 6(g)] reveals the ring pattern corresponding to the real oak ring image. Note that the IA estimated via the DHODA [Fig. 6(h)] suffers from the same issue, whereas the IA estimated via the BMFT-DHODA [Fig. 6(i)] does not. Based on the observation, we see that ESA demodulation such as that employed by the DHODA prohibits its direct application to wideband real images due to the narrowband and estimation range constraints, while the proposed BMFT framework overcomes such constraints and allows for direct application of ESA demodulation to wideband real images.

8. CONCLUSION

In this paper, we have formally defined the notion of locally wideband FM images and the corresponding local modulation index. We extended the 1D approach combining multirate frequency transformations and energy demodulation to 2D and images by using their separable counterparts. The proposed algorithm was applied to both synthetic and real images and shown to produce significant reduction in the demodulation errors. The proposed approach was shown to be effective in cases where the existing algorithms are limited in terms of their estimation range.

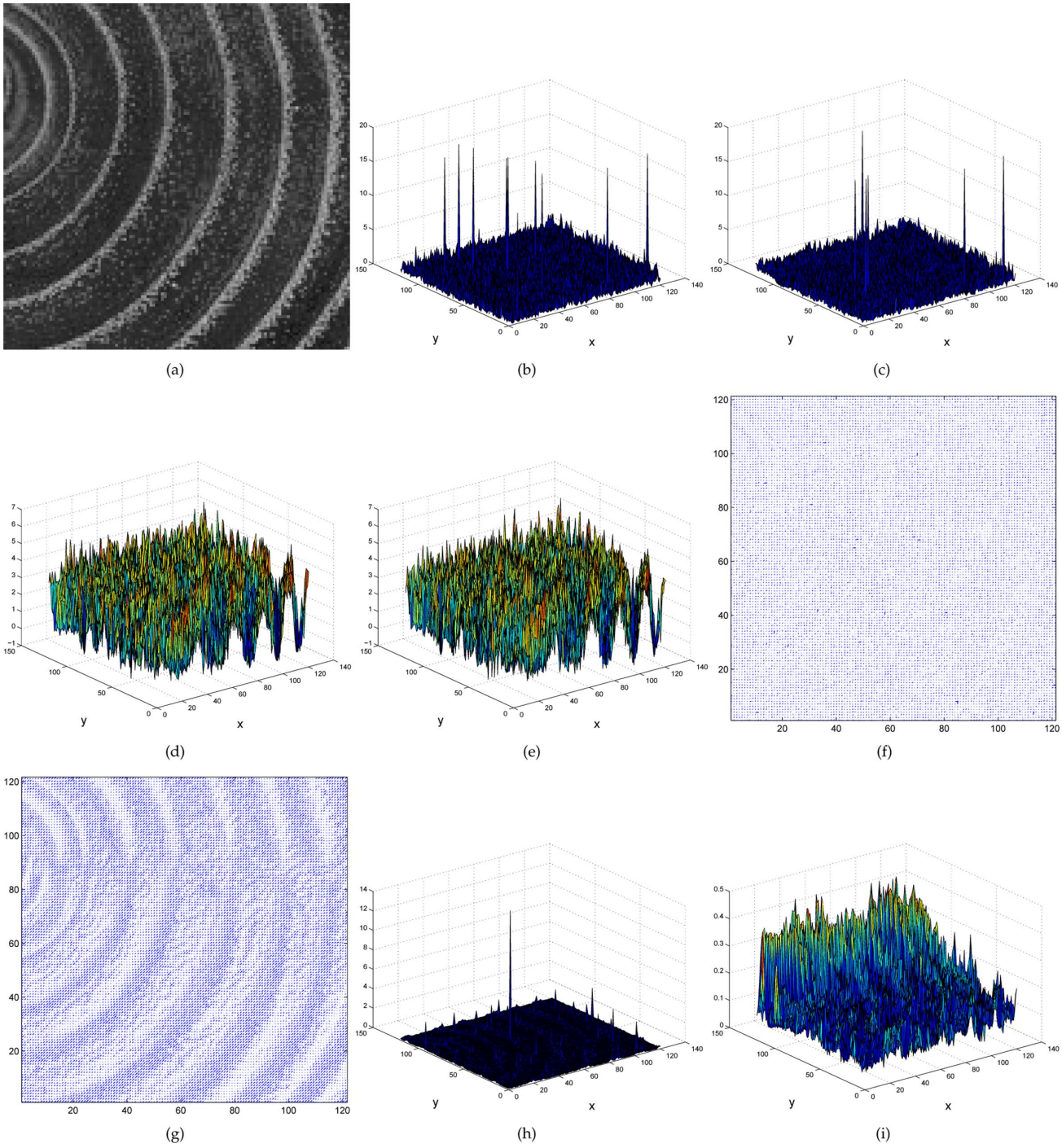

Fig. 6. Demodulation of the oak ring image (photo by H. D. Grissino-Mayer). (a) Real image of the oak ring, (b) estimation of the IF component along the horizontal direction via the DHODA, (c) estimation of the IF component along the vertical direction via the DHODA, (d) estimation of the IF component along the horizontal direction via the BMFT-DHODA, (e) estimation of the IF component along the vertical direction via the BMFT-DHODA, and (f) estimation of the IF needle plot via the DHODA. (g) Estimation of the IF needle plot via the BMFT-DHODA. (h) Estimation of the IA via the DHODA. (i) Estimation of the IA via the BMFT-DHODA. Note that the conversion factors of the BMFT-DHODA here are $\mathbf{R} = \mathrm{diag}[16, 16]$.

APPENDIX A: ERROR ANALYSIS FOR EXTREMELY WIDEBAND FM SIGNAL

Here we present the error analysis for wideband sinusoidal FM demodulation in 1D. (Since the partial Hilbert transform is a separable combination of the 1D Hilbert transforms, consequently, this analysis is valid for the proposed 2D approach as well.) According to the handbook of mathematic formula and basic trigonometric identities, we have

$$\cos(\beta \sin\theta) = J_0(\beta) + 2\sum_{k=1}^{\infty} J_{2k}(\beta)\cos(2k\theta),$$

$$\sin(\beta \sin\theta) = 2\sum_{k=0}^{\infty} J_{2k+1}(\beta)\sin((2k+1)\theta),$$

$$\cos(u)\cos(v) = \frac{1}{2}[\cos(u-v) + \cos(u+v)],$$

$$\sin(u)\sin(v) = \frac{1}{2}[\cos(u-v) - \cos(u+v)],$$

where $J_n(\beta)$ denotes the Bessel function of the first kind.

Using the above equations, the sinusoidal FM can be expanded as

$$\begin{aligned}
&\cos(\omega_c t + \beta \sin(\omega_m t)) \\
&= \cos(\omega_c t)\cos(\beta \sin(\omega_m t)) - \sin(\omega_c t)\sin(\beta \sin(\omega_m t)) \\
&= \cos(\omega_c t)J_0(\beta) + 2\sum_{k=1}^{\infty} J_{2k}(\beta)\cos(2k\omega_m t)\cos(\omega_c t) \\
&\quad - 2\sum_{k=0}^{\infty} J_{2k+1}(\beta)\sin((2k+1)\omega_m t)\sin(\omega_c t) \\
&= \cos(\omega_c t)J_0(\beta) + 2\sum_{k=1}^{\infty} J_{2k}(\beta)\cos((\omega_c + 2k\omega_m)t) \\
&\quad + 2\sum_{k=1}^{\infty} J_{2k}(\beta)\cos((\omega_c - 2k\omega_m)t) \\
&\quad + 2\sum_{k=0}^{\infty} J_{2k+1}(\beta)\cos((\omega_c t + (2k+1)\omega_m)t) \\
&\quad - 2\sum_{k=0}^{\infty} J_{2k+1}(\beta)\cos((\omega_c - (2k+1)\omega_m)t).
\end{aligned}$$

Its quadrature part we desire for demodulation can also be expanded similarly given by

$$\begin{aligned}
&\sin(\omega_c t + \beta \sin(\omega_m t)) \\
&= \sin(\omega_c t)\cos(\beta \sin(\omega_m t)) + \cos(\omega_c t)\sin(\beta \sin(\omega_m t)) \\
&= \sin(\omega_c t)J_0(\beta) + 2\sum_{k=1}^{\infty} J_{2k}(\beta)\cos(2k\omega_m t)\sin(\omega_c t) \\
&\quad + 2\sum_{k=0}^{\infty} J_{2k+1}(\beta)\sin((2k+1)\omega_m t)\cos(\omega_c t) \\
&= \sin(\omega_c t)J_0(\beta) + 2\sum_{k=1}^{\infty} J_{2k}(\beta)\sin((\omega_c + 2k\omega_m)t) \\
&\quad + 2\sum_{k=1}^{\infty} J_{2k}(\beta)(\sin(\omega_c - 2k\omega_m)t) \\
&\quad + 2\sum_{k=0}^{\infty} J_{2k+1}(\beta)\sin((\omega_c t + (2k+1)\omega_m)t) \\
&\quad - 2\sum_{k=0}^{\infty} J_{2k+1}(\beta)\sin((\omega_c - (2k+1)\omega_m)t).
\end{aligned}$$

Note that the Hilbert transform of the corresponding sinusoidal FM can be easily obtained by performing the Hilbert transform at each of its harmonics as

$$\begin{aligned}
&\mathcal{H}[\cos(\omega_c t + \beta \sin(\omega_m t))] \\
&= \sin(\omega_c t)J_0(\beta) + 2\sum_{k=1}^{\infty} J_{2k}(\beta)\sin(\omega_c + 2k\omega_m)t) \\
&\quad + 2\sum_{k=1}^{\infty} J_{2k}(\beta)\sin(|\omega_c - 2k\omega_m|t) \\
&\quad + 2\sum_{k=0}^{\infty} J_{2k+1}(\beta)\sin((\omega_c + (2k+1)\omega_m)t) \\
&\quad - 2\sum_{k=0}^{\infty} J_{2k+1}(\beta)\sin(|\omega_c - (2k+1)\omega_m|t).
\end{aligned}$$

By comparing the quadrature and the Hilbert transform of the corresponding sinusoidal FM, we observe that when $\omega_c < n\omega_m$,

$$\mathcal{H}[\cos((\omega_c - n\omega_m)t)] = \sin(n\omega_m - \omega_c)t,$$

whereas the corresponding term in the quadrature part is of opposite sign $\sin(\omega_c - n\omega_m)t$. For narrowband sinusoidal FM, the Bessel coefficients $J_n(\beta)$ associated with these corresponding side lobes are very small, and the demodulation error incurred by the Hilbert transform due to these opposite sign terms can be neglected. Hence, the Hilbert transform provides almost perfect reconstruction of the quadrature part we desire for demodulation using the analytic signal for sinusoidal FM in the narrowband case. For extremely wideband sinusoidal FM, however, due to its large modulation index β, the Bessel coefficients associated with these side lobes cannot be neglected anymore. As a result, the error incurred by the Hilbert transform is much more significant. In general, this unavoidable error imposes a lower bound on the error performance for HT and energy operator in the extremely wideband scenario.

Funding. Air Force Research Laboratory (AFRL) (FA9453-14-1-0234).

REFERENCES

1. J. G. Daugman and C. J. Downing, "Demodulation, predictive coding, and spatial vision," J. Opt. Soc. Am. A **12**, 641–660 (1995).
2. M. Pattichis, G. Panayi, A. Bovik, and S.-P. Hsu, "Fingerprint classification using an AM-FM model," IEEE Trans. Image Process. **10**, 951–954 (2001).
3. J. Havlicek, D. Harding, and A. Bovik, "Discrete quasi-eigenfunction approximation for AM-FM image analysis," in *Proceedings of International Conference on Image Processing* (IEEE, 1996), pp. 633–636.
4. A. Bovik, N. Gopal, T. Emmoth, and A. Restrepo, "Localized measurement of emergent image frequencies by gabor wavelets," IEEE Trans. Inf. Theory **38**, 691–712 (1992).
5. N. E. Huang, *Hilbert-Huang Transform and Its Applications* (World Scientific, 2014).
6. J. Havlicek, J. Havlicek, and A. Bovik, "The analytic image," in *Proceedings of International Conference on Image Processing* (IEEE, 1997), pp. 446–449.
7. P. Maragos and A. C. Bovik, "Image demodulation using multidimensional energy separation," J. Opt. Soc. Am. A **12**, 1867–1876 (1995).
8. I. Kokkinos, G. Evangelopoulos, and P. Maragos, "Advances in texture analysis: energy dominant component multiple hypothesis testing," in *Proceedings of International Conference on Image Processing* (IEEE, 2004), pp. 1509–1512.

9. V. Murray, P. Rodriguez, and M. Pattichis, "Multiscale AM-FM demodulation and image reconstruction methods with improved accuracy," IEEE Trans. Image Process. **19**, 1138–1152 (2010).
10. K. Larkin, D. Bone, and M. Oldfield, "Natural demodulation of two-dimensional fringe patterns. I. General background of the spiral phase quadrature transform," J. Opt. Soc. Am. A **18**, 1862–1870 (2001).
11. K. Larkin, "Natural demodulation of two-dimensional fringe patterns. II. Stationary phase analysis of the spiral phase quadrature transform," J. Opt. Soc. Am. A **18**, 1871–1881 (2001).
12. M. Unser, D. Sage, and S. Van De Ville, "Multiresolution monogenic signal analysis using the Riesz-Laplace wavelet transform," IEEE Trans. Image Process. **18**, 2402–2418 (2009).
13. M. Gupta and B. Santhanam, "Adaptive linear predictive frequency tracking and cpm demodulation," in *Thirty-Seventh Asilomar Conference on Signals, Systems and Computers* (IEEE, 2003), pp. 202–206.
14. A. Potamianos and P. Maragos, "A comparison of the energy operator and the Hilbert transform approach to signal and speech demodulation," Signal Process. **37**, 95–120 (1994).
15. M. Pattichis and A. Bovik, "Analyzing image structure by multidimensional frequency modulation," IEEE Trans. Pattern Anal. Mach. Intell. **29**, 753–766 (2007).
16. J. Havlicek, J. Havlicek, N. Mamuya, and A. Bovik, "Skewed 2D Hilbert transforms and computed AM-FM models," in *Proceedings of International Conference on Image Processing* (IEEE, 1998), pp. 602–606.
17. A. Bovik, M. Clark, and W. Geisler, "Multichannel texture analysis using localized spatial filters," IEEE Trans. Pattern Anal. Mach. Intell. **12**, 55–73 (1990).
18. F. Salzenstein, A.-O. Boudraa, and J.-C. Cexus, "Generalized higher-order nonlinear energy operators," J. Opt. Soc. Am. A **24**, 3717–3727 (2007).
19. E.-H. Diop, A. Boudraa, and F. Salzenstein, "Higher order Teager-Kaiser operators for image analysis: part I—a monocomponent image demodulation," in *Proceedings of International Conference on Acoustics, Speech and Signal Processing* (IEEE, 2009), pp. 1041–1044.
20. E.-H. S. Diop and A. O. Boudraa, "Higher order Teager-Kaiser operators for image analysis: PART II—a multicomponent image demodulation," in *Proceedings of International Conference on Image Processing* (IEEE, 2009), pp. 1357–1360.
21. P. Maragos and A. Potamianos, "Higher order differential energy operators," IEEE Signal Process. Lett. **2**, 152–154 (1995).
22. B. Santhanam and P. Maragos, "Energy demodulation of two-component AM-FM signal mixtures," IEEE Signal Process. Lett. **3**, 294–298 (1996).
23. B. Santhanam, "Generalized energy demodulation for large frequency deviations and wideband signals," IEEE Signal Process. Lett. **11**, 341–344 (2004).
24. F. Salzenstein and A. O. Boudraa, "Multi-dimensional higher order differential operators derived from the Teager-Kaiser energy-tracking function," Signal Process. **89**, 623–640 (2009).
25. F. Salzenstein, A. O. Boudraa, and T. Chonavel, "A new class of multi-dimensional Teager-Kaiser and higher order operators based on directional derivatives," Multidimens. Syst. Signal Process. **24**, 543–572 (2013).
26. W. Liu and B. Santhanam, "Wideband-fm demodulation for large wideband to narrowband conversion factors via multirate frequency transformations," in *Proceedings of Signal Processing and Signal Processing Education Workshop* (IEEE, 2015), pp. 7–12.